

# Chiral microwave nonreciprocity demonstrated via Rayleigh and Sezawa modes supported in an $\text{Al}_{0.58}\text{Sc}_{0.42}\text{N}/4\text{H-SiC}$ platform

A.R. Will-Cole<sup>1,\*</sup>, Xingyu Du<sup>2</sup>, Bin Luo<sup>3</sup>, Valeria Lauter<sup>4</sup>, Alexander Grutter<sup>5</sup>,  
 Lisa Hackett<sup>1</sup>, Michael Miller<sup>1</sup>, Yuanchen Deng<sup>1</sup>, Brandon Smith<sup>1</sup>, Olivia Pitcl<sup>6</sup>, Nian X. Sun,<sup>3</sup>  
 Roy H. Olsson III<sup>2</sup> and Matt Eichenfield<sup>1,6,†</sup>

<sup>1</sup>Microelectronics engineering, systems, and applications, Sandia National Laboratories, Albuquerque 87115, NM


<sup>2</sup>Department of Electrical and Systems Engineering, The University of Pennsylvania, Philadelphia, Pennsylvania, USA

<sup>3</sup>Department of Electrical Engineering, Northeastern University, Boston, Massachusetts, USA

<sup>4</sup>Neutron Sciences Division, Oak Ridge National Laboratory, Oak Ridge, Tennessee, 37831, USA

<sup>5</sup>NIST Center for Neutron Research, National Institute of Standards and Technology, Gaithersburg, Maryland, 20899, USA

<sup>6</sup>Wyant College of Optical Sciences, The University of Arizona, Tucson, Arizona 85721, USA

 (Received 5 December 2024; revised 6 February 2025; accepted 28 February 2025; published 24 March 2025)

Chirality plays a crucial role in the helicity mismatch between surface acoustic waves and magnetic spin waves, leading to nonreciprocal transmission of acoustic power for coupled magnetoacoustic modes. Acoustic modes with both longitudinal and shear strain exhibit elliptical particle displacements, making them chiral, and different acoustic modes can exhibit different helicities of this elliptical particle displacement. Here, we study chiral acoustic modes with different helicities supported on the same piezoelectric platform and their interaction with magnetic spin waves. Our study demonstrates that the nonreciprocal transmission of acoustic power is driven by the helicity mismatch effect and, specifically, that the handedness of the nonreciprocity is based on whether the surface acoustic wave has retrograde (Rayleigh mode) or prograde (Sezawa mode) elliptical particle displacement with respect to the propagation direction. We found the transmission nonreciprocity to be significant, with 7.3 dB/mm for the retrograde particle displacement (Rayleigh mode at 2.358 GHz) and 3.3 dB/mm for prograde particle displacement (Sezawa mode at 3.112 GHz). This work highlights that piezoelectric platforms can be engineered to support acoustic modes with opposite helicities to enable frequency-selective nonreciprocal radiofrequency and microwave components, such as isolators and circulators, through coupled acoustic spin wave interactions.

DOI: [10.1103/PhysRevApplied.23.034058](https://doi.org/10.1103/PhysRevApplied.23.034058)

## I. INTRODUCTION

Chirality is a fundamental property observed when an object cannot be superimposed onto its mirror image through rotation and translation alone [1], such as the right-handed helical structure of DNA [2,3], chiral structure of proteins comprised of L-amino acids [4,5], electromagnetic chirality of circularly polarized light [6,7], etc. Surface acoustic wave (SAW) modes with both longitudinal and shear strain have elliptical particle motion, for example, a Rayleigh wave, and this ellipticity defines a chirality or handedness that is perpendicular to the wave's propagation direction [8]. For linear, time-invariant media, SAW propagation is reciprocal [9]. Magnetic spin waves, on the other hand, are inherently achiral, and

their propagation is also reciprocal. However, if symmetry is broken out-of-plane through interfacial effects or asymmetric exchange interactions, magnetic spin waves with in-plane propagation become nonreciprocal [10]. In the case of acoustic-driven magnetic resonance (ADMR), whereby SAWs interact with magnetic spin waves to form hybridized magnetoacoustic modes, there is one inherent source of nonreciprocity driven by the differing helicities that cause the waves to have relatively weaker or stronger coupling depending on the propagation direction [11]. This is referred to as the helicity mismatch effect and has been experimentally observed in a variety of systems, including coupling between a Rayleigh mode and magnetic spin waves in Ga-doped  $\text{Y}_3\text{Fe}_5\text{O}_{12}$  [12], Ni [13], and Ta/CoFeB/MgO systems [14]. Figure 1 shows a schematic of the anticipated magnetic absorption pattern and nonreciprocity driven by the helicity mismatch effect. In certain systems, the strength of the nonreciprocity was

\*Contact author: [arwillc@sandia.gov](mailto:arwillc@sandia.gov)

†Contact author: [eichenfield@arizona.edu](mailto:eichenfield@arizona.edu)

not fully described by the helicity mismatch effect driven only by magnetoelastic coupling. Rather, it also required the contribution of magnetorotational coupling, where the rotational motion couples with the magnetization via magnetic anisotropies. This was originally predicted by Maekawa and Tachiki and, more recently, experimentally demonstrated by Xu *et al.* in a Ta/CoFeB/MgO system with perpendicular magnetic anisotropy [14–16]. Disentangling individual contributions such as magnetorotational coupling [15,16], spin-rotational coupling [17,18], and gyromagnetic coupling [19] poses a challenge due to their overlapping symmetries with respect to the magnetoelastic driving field [11].

Recently, there has been heightened attention on SAW-spin-wave coupled devices due to this observed microwave nonreciprocity [11,20,21]. While the helicity mismatch between the SAWs and magnetic spin waves leads to nonreciprocity, greatly enhanced nonreciprocity can be achieved through the integration of magnetic heterostructures with strong asymmetry in their spin wave dispersion, i.e., synthetic antiferromagnetic heterostructures, and those with interfacial Dzyaloshinskii-Moriya interactions [22–28]. This results in both nonreciprocal acoustic power transmission and phase accumulation [24]. Figure 1 displays a schematic highlighting the anticipated magnetic absorption and nonreciprocal transmission for ADMR devices, where the nonreciprocity is dominated by asymmetric spin wave dispersions. Of course, in a physical system with the nonreciprocity driven primarily asymmetric spin wave dispersions, there will also be some minor contribution from the helicity mismatch effect. SAW-asymmetric spin-wave-coupled devices show promise for radiofrequency front-end components, such as isolators and circulators [28]. Thus, the study of nonreciprocal coupling between SAWs and magnetic spin waves is of significant technological relevance.

Here, we specifically engineered a piezoelectric platform of a 1- $\mu\text{m}$   $\text{Al}_{0.58}\text{Sc}_{0.42}\text{N}$  (AlScN) film on 4H-SiC to support two acoustic modes with opposite helicities, specifically a Rayleigh mode and a Sezawa mode, that are excited with the same transducer. This acoustic platform has several unique advantages. It has (1) a high piezoelectric transduction efficiency for the Sezawa acoustic mode, (2) isotropic acoustic propagation in the plane (which eases on-chip design compared with anisotropic platforms, e.g.,  $\text{LiNbO}_3$ ), and (3) high thermal conductivity, which is necessary for any rf transmitter operation that generally uses hundreds of milliwatts or even watts of power [29,30]. This platform also has high resistivity, low rf losses, and low acoustic propagation losses [29–31]. The velocity contrast between 4H-SiC and AlScN for all Sc-doping concentrations has been shown to support strongly guided slab modes [29,30,32,33], and the high acoustic velocity of the strongly electromechanically coupled modes of the stack support operation at higher

frequencies than typical materials using  $\text{LiNbO}_3$ . In addition, this platform is of increasing technological relevance as acoustoelectric amplifiers with a gain of 500 dB/cm have recently been demonstrated [34].

## II. MAGNETIC HETEROSTRUCTURE CHARACTERIZATION

Magnetic heterostructures for ADMR should have high magnetostriction to optimize the strain coupling with the piezoelectric film, low magnetic damping for low coupled losses, and high magnetization such that lower applied magnetic fields are required for resonance [21]. For this study, we selected  $(\text{Fe}_{81}\text{Ga}_{19})_{88}\text{B}_{12}$  (FeGaB), specifically a heterostructure of FeGaB/ $\text{SiO}_2$ /FeGaB, due to its high saturation magnetostriction of 70 ppm, narrow ferromagnetic resonance linewidth of  $<20$  Oe in the X-band, and high saturation magnetization (14 500 Gauss) [35–37]. To assess the magnetization of each respective FeGaB layer in our heterostructure and to ensure we did not have interfacial chemical mixing, we conducted polarized neutron reflectometry at the Spallation Neutron Source at Oak Ridge National Laboratory [38]. Polarized neutron reflectometry (PNR) is a technique that provides through-thickness depth profiles of the nuclear (real  $\rho_N$  and imaginary  $\rho_{N,i}$ ) and magnetic ( $\rho_M$ ) scattering length densities (SLD), referred to as nuclear SLD and magnetic SLD, respectively, within the heterostructure [39]. The real part of the nuclear SLD depends on the material’s density and composition, while the imaginary part is associated with the absorption SLD and the magnetic SLD is directly associated with the net in-plane magnetization [38–41]. From a fitting of the PNR data, the depth-resolved information on the composition, density, and magnetization of the heterostructure is obtained [39–41]. Measurements were performed in ambient conditions with an electromagnet to apply a magnetic field. For the PNR measurement, a spin-polarized neutron beam with a wavelength band  $\lambda$  (2.5–8.5 Å) was incident on the sample at a grazing incidence angle,  $\theta$ , while a spin flipper was used to alternate the incoming neutron spin state. The spin-dependent neutron reflectivity spectra,  $R^+$  and  $R^-$ , were measured as a function of the wavevector transfer,  $Q = 4\pi \sin(\theta)/\lambda$ , along the direction normal to the film surface. The measurements were collected at 300 K with an in-plane magnetic field of 1 T, far exceeding the saturation of the sample [35]. The PNR samples were fabricated on a silicon substrate with a 10 mm  $\times$  10 mm cross-sectional area to reduce the neutron count time required for high- $Q$  measurements. The data was fit using the ReFl-1D software package [42]. The PNR reflectivity, spin asymmetry, and the nuclear and magnetic SLDs are given in Figs. 2(a)–2(c). The PNR analysis revealed the respective FeGaB layer thicknesses were 167.72(35) and 149.34(32) Å, respectively,

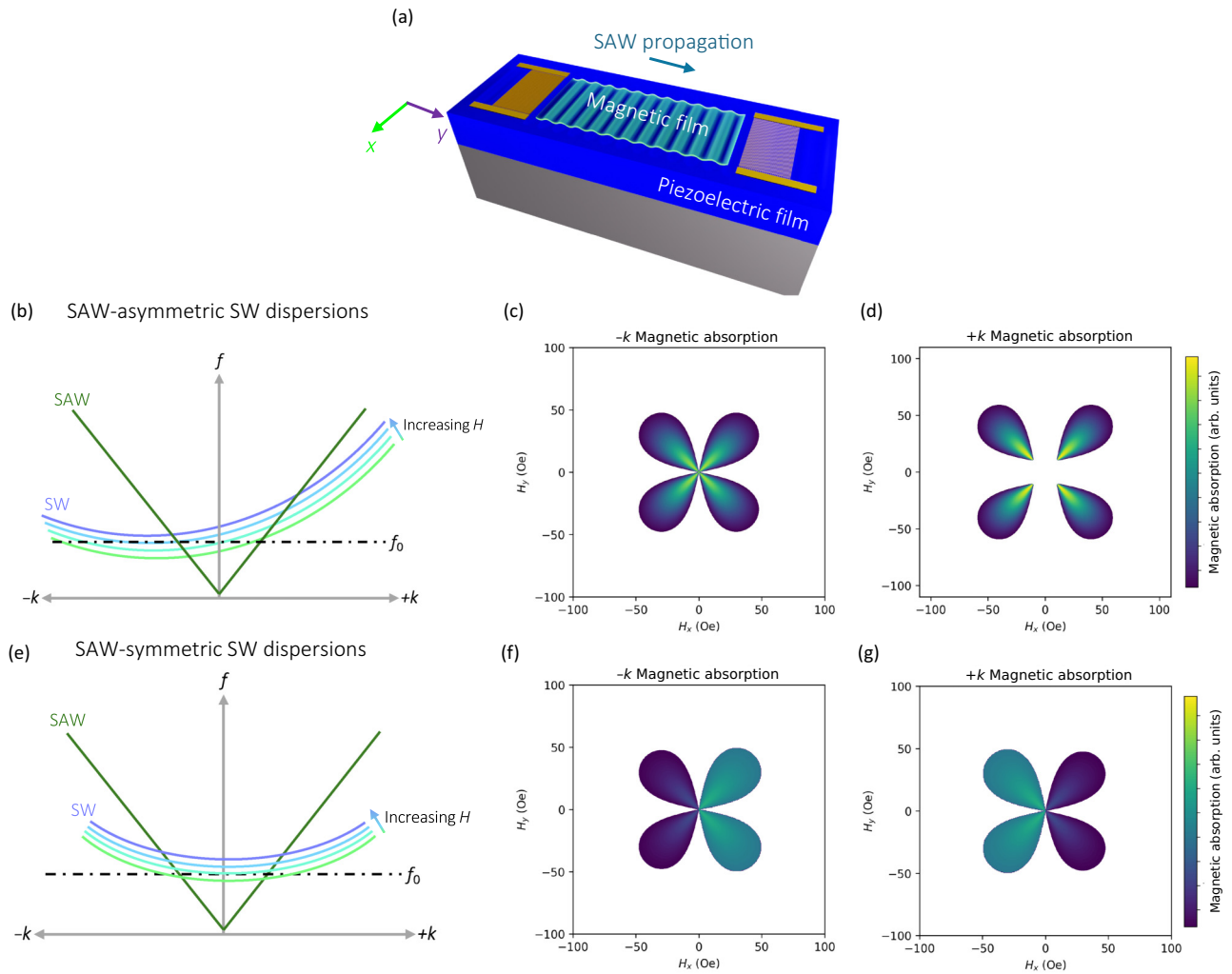


FIG. 1. A conceptual diagram of the two main drivers of nonreciprocal transmission for acoustic-driven magnetic resonance (ADM) devices, where  $f$  is defined as frequency,  $k$  is the propagation vector, and  $H$  is the dc magnetic field. (a) Rendering of a surface acoustic wave (SAW) delay line coupled to a magnetic film. In this diagram, the SAW propagation axis ( $+k$  and  $-k$ ) is defined along the  $y$ -axis. The vector magnetic field is applied in the  $xy$ -plane (components  $H_x$  and  $H_y$ ). The coupling between the SAW-spin wave (SW) can be understood via the SAW-SW dispersion relation. Note that the SAW dispersion is linear and symmetric and the SW dispersion varies based on the applied magnetic field bias field (represented here as curves from light green to light purple). (b) Diagram of the SAW-SW dispersion (SAW labeled in green and SW labeled in light purple) in the case of an asymmetric spin wave dispersion. The asymmetric spin wave dispersion could result from strong interlayer coupling or an antisymmetric exchange interaction. (c),(d) Anticipated magnetic absorption as a function of the applied in-plane magnetic field ( $H_x$ ,  $H_y$ ). Here, the resonance field required for the SAW-SW coupling is different for the same operation frequency based on the SAW propagation direction ( $+k$  versus  $-k$ ). If the nonreciprocity is caused purely by the asymmetric spin wave dispersion, and the SAW dispersion remains linear and symmetric, the interaction can be nonreciprocal but not necessarily chiral. (e) Diagram of the SAW-SW dispersion given in the case of a symmetric spin wave dispersion (SAW labeled in green and SW labeled in light purple). (f),(g) Corresponding anticipated behavior for nonreciprocity driven primarily via helicity mismatch effect, which would be the case here. (d) Example of the dispersion relation for reciprocal spin-wave and SAW, but the coupling is stronger or weaker for  $+k$  or  $-k$  based on the helicity mismatch effect for a particular applied field magnetic field shown in (e),(f). Note that these diagrams are conceptual and exaggerated to emphasize the differences between the two drivers of nonreciprocity in ADMR. In the case of the helicity mismatch effect in (e)–(g), the magnetic absorption pattern lacks rotational symmetry due to the asymmetric coupling strengths and, therefore, is chiral.

and the  $\text{SiO}_2$  spacer thickness was  $37.96(18) \text{ \AA}$ . The sensitivity of neutrons to boron due to its absorption cross section is an additional advantage and allows precise determination of the depth profile of the boron distribution. We found FeGaB layers with magnetic scattering

densities of  $3.173(20) \times 10^{-6}$  and  $3.421(20) \times 10^{-6} \text{ \AA}^{-2}$ , respectively, corresponding to 1111 kA/m (13 971 Gauss) and 1198 kA/m (15 063 Gauss)—these magnetic scattering length densities were uniform through the respective layer thicknesses. This high magnetization is close to the

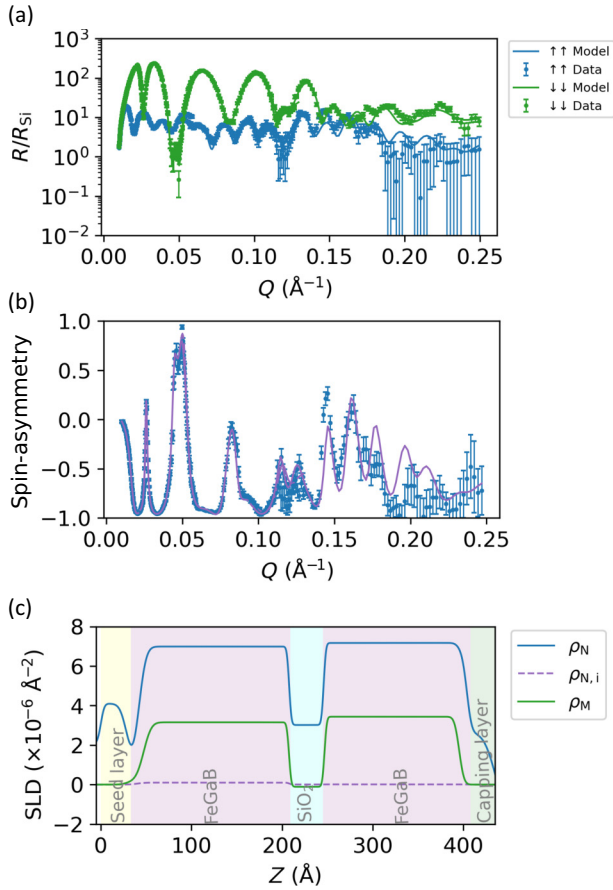


FIG. 2. (a) Reflectivity normalized by the theoretical reflectivity of a Si substrate for both spin-up and spin-down neutrons along with their model fit, (b) Spin asymmetry along with the model fit. In (a),(b), the error bars represent  $\pm 1$  standard deviation. (c) Model profile for nuclear and magnetic scattering length density.

approximate 1153 kA/m (14 500 Gauss) expected for 12% B-content, the desired FeGaB composition [35].

We also performed broadband ferromagnetic resonance (FMR) measurements to better characterize the magnetic loss of the magnetic heterostructure. FMR measurements were performed with a swept bias field that yielded differential absorption spectra at each frequency,  $f$ , where the derivative peak corresponds to the main resonance uniform mode. The measurements were taken in a transverse pumping geometry to favor the acoustic mode [43]. The measurement frequency varied from 2.5 to 31 GHz, and the sample temperature was held at 298 K. The FMR spectrum is shown in Fig. 3(a). One uniform mode was observed until approximately 12 GHz, where the mode begins to split into two resonances—see Fig. 3(b). The split resonances indicate there may be a variation between the effective magnetizations, likely due to variations in the magnetic layer magnetizations and anisotropies. The variation in magnetization between the FeGaB layers is

consistent with the PNR measurements and analysis. To account for this in our analysis, we fit the derivative of a single Lorentzian to our data below 12 GHz while, for above 12 GHz, we fit the derivative of the sum of two Lorentzians to effectively capture the individual layer resonances. The effective in-plane magnetization and gyromagnetic ratio were extracted from the FMR data using the Kittel equation, i.e.,

$$f = |\gamma/2\pi| \sqrt{H_{\text{res}}(H_{\text{res}} + 4\pi M_{\text{eff}})}, \quad (1)$$

where  $H_{\text{res}}$  is the resonance field,  $\gamma$  is the gyromagnetic ratio, and  $4\pi M_{\text{eff}}$  is the effective in-plane magnetization.

The results of the Kittel fit are shown in Fig. 3(d). The gyromagnetic ratio is higher than the expected 28 GHz/T value, likely due to inhomogeneity in the FeGaB films as evidenced by the different magnetization values and inhomogeneity-induced FMR peak broadening, which shows up only in the low-field regime (this is not present at frequencies  $> 12$  GHz and the corresponding higher applied magnetic field). The Gilbert damping constant and inhomogeneous broadening were extracted from a linear fit of the full-width half-maxima of the Lorentzian as a function of frequency. We limited this analysis to below 10 GHz to ensure that we were only fitting to a single resonance. We extracted this quantitative information using the following expression:

$$\Delta H_{\text{FWHM}} = \Delta H_0 + 2\pi\alpha/\gamma \quad (2)$$

where  $\Delta H_{\text{FWHM}}$  is the uniform mode linewidth,  $\Delta H_0$  is the inhomogeneous linewidth broadening,  $\alpha$  is the Gilbert damping constant, and  $\gamma$  is the gyromagnetic ratio (extracted from the Kittel equation).

The results for the Gilbert damping fit are shown in Fig. 3(e). Overall, the FMR measurement and analysis indicate that there is a high effective magnetization (i.e., approximately 13 000 and 12 700 Gauss for the two FeGaB layers), negligible inhomogeneous broadening (1.62 Oe), and low damping ( $6.10 \times 10^{-3}$ ) and, therefore, ultralow magnetic loss.

### III. PIEZOELECTRIC PLATFORM DESIGN AND OPTIMIZATION

Most ADMR devices to date have focused on Rayleigh modes [21], which have both longitudinal and vertical shear components, creating a retrograde elliptical motion of surface particles relative to the SAW propagation direction [44–46]. A Sezawa mode, a higher-order Rayleigh wave, is supported in multilayered structures, typically when a lower-velocity piezoelectric layer is deposited on a higher-velocity substrate [29,30,34]. This requirement makes forming a guided structure with AlN or AlScN

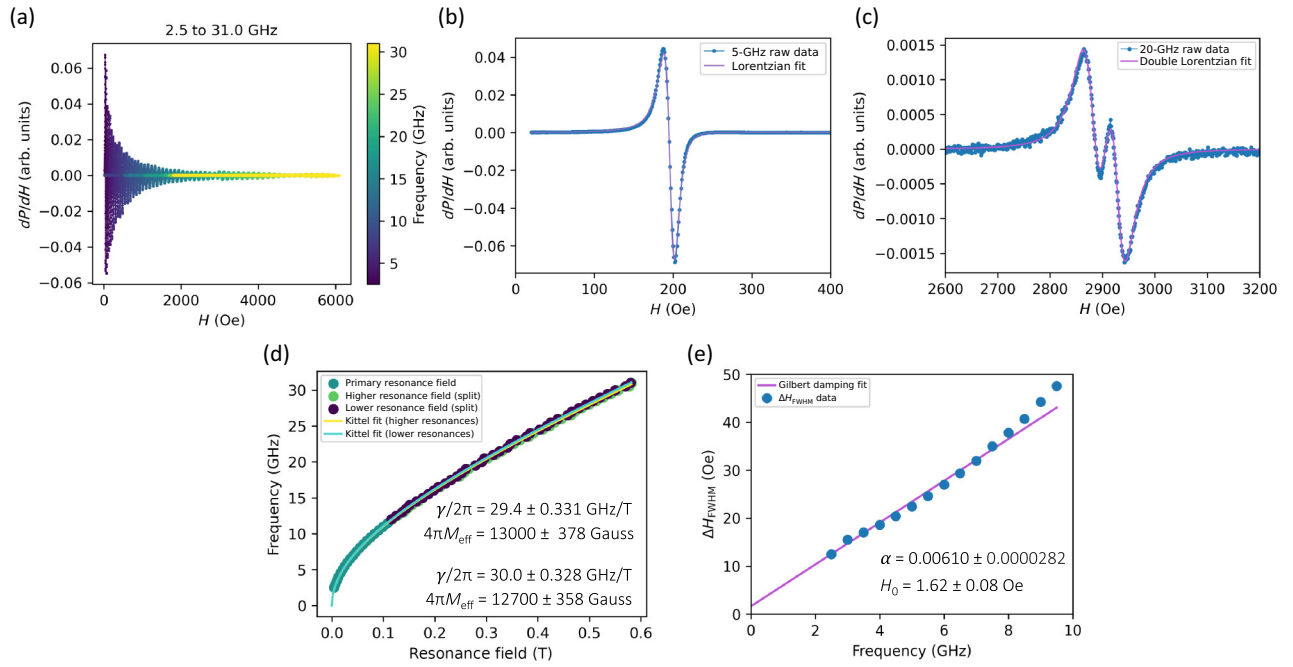


FIG. 3. (a) Raw ferromagnetic resonance characterization from 2.5 to 31.0 GHz in the transverse pumping geometry; thus, these are the acoustic mode resonances. (b) 5-GHz raw data with a single Lorentzian derivative fit and (c) 20-GHz raw data with a double Lorentzian derivative fit to fully capture the slight difference in resonance fields between the two respective FeGaB film layers. (d) Kittel fit considering slight variation in the resonance fields for the two respective films in the bilayer at higher frequencies with fitted values displayed. (e) Resonance linewidth (full-width half-maximum) versus frequency below the resonance splitting with the Gilbert damping fit plotted and values displayed.

challenging because these piezoelectric materials have a high acoustic velocity. However, 4H-SiC has longitudinal and shear velocities of approximately 13 and 7 km/s [47], respectively, that have sufficiently high velocities to support a guided mode with the AlScN piezoelectric film. The Sezawa mode is confined to the surface while still interacting with the substrate interface and exhibits a prograde elliptical trajectory of surface particles relative to the SAW propagation direction [46]. While the Rayleigh mode has been extensively studied in the context of coupling with magnetic spin waves, the Sezawa mode has not received as much attention in this field [48,49]. In this work, we have engineered our AlScN/SiC heterostructure specifically to support both the Rayleigh (retrograde ellipticity) and Sezawa (prograde ellipticity) modes by tuning the layer thickness and velocity mismatch, enabling us to access different SAW helicities in our ADMR experiments. To our knowledge, nonreciprocity enabled by SAW-spin-wave helicity mismatch has not been studied on the AlScN/SiC platform to directly probe the effect of two SAW polarizations, i.e., the Rayleigh (retrograde ellipticity) and Sezawa (prograde ellipticity) modes.

The 1- $\mu\text{m}$  AlScN films were deposited on SiC substrates, as reported previously [29,30], and the films are of high crystalline quality, which is evident by the full-width

half-maximum of the x-ray diffraction rocking curve of  $1.05^\circ$  for the AlScN (0002)-peak (refer to Supplemental Material 1) [50]. Based on the anticipated magnetic field required for SAW-SW coupling in this system (see Supplemental Material 2) [50,51] and the maximum magnetic field on our probe station, we required a target operation frequency of 3 GHz for the Sezawa mode. We performed an eigenmode simulation using COMSOL finite element modeling of the Rayleigh and Sezawa mode, assuming a 1- $\mu\text{m}$  AlScN film on SiC—see Fig. 4. Assuming a wavelength of 2.222  $\mu\text{m}$ , the simulation revealed that the Sezawa mode supported on our piezoelectric platform has a phase velocity of approximately 6666 m/s. We ran our simulation for several wavelengths and calculated the frequency of the Rayleigh and Sezawa eigenmodes and were able to map out the dispersion of the modes—see Fig. 4(c). The phonon dispersion of both the Rayleigh and Sezawa modes is linear in the relevant wavelength regimes presented here.

A SAW delay line device consists of metal interdigital transducers (IDTs) on a piezoelectric film or substrate. The electrical energy applied to the IDTs is converted into an acoustic wave via the inverse piezoelectric effect. The SAW wavelength ( $\lambda_{\text{SAW}}$ ) is determined by the periodicity of the IDTs and the frequency of operation is approximated by the ratio of the acoustic wave velocity to the

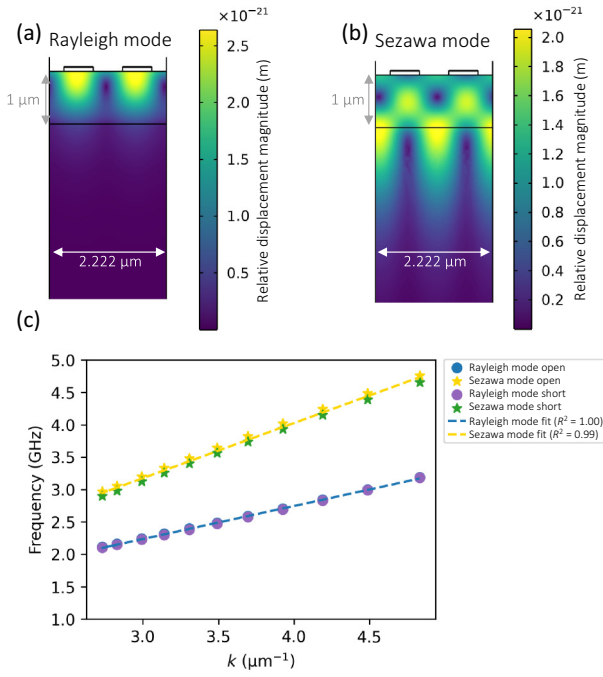


FIG. 4. COMSOL finite element model eigenmode simulation of the (a) Rayleigh and (b) Sezawa modes for the AlScN/SiC platform in the transducer region. (c) Simulated dispersion for the Rayleigh and Sezawa modes.

SAW wavelength ( $v_a/\lambda_{\text{SAW}}$ )—noting that  $v_a$  is dependent on wavelength and thickness. Using the results from the eigenmode simulation, we used a wavelength of  $2.222 \mu\text{m}$  to design our bidirectional IDTs, where the transducer finger width and spacing were targeted to be  $\lambda_{\text{SAW}}/4$ . We optimized the SAW device IDT design experimentally through a parameter sweep of the number of transducer finger pairs and the transducer aperture (refer to Supplemental Material 3) [50]. Apertures of  $50\lambda_{\text{SAW}}$  and  $75\lambda_{\text{SAW}}$  with 10–50 transducer finger pairs and a delay length of  $50 \mu\text{m}$  yielded a Sezawa mode with close to 6 dB of insertion loss, which is the absolute minimum possible with bidirectional IDTs and indicates very low excess loss from our design. We experimentally determined the average propagation loss for the Sezawa mode by measuring the minimum insertion loss across delays of 50, 250, 500, and  $750 \mu\text{m}$  as a function of the device aperture and found a loss of 8.48 dB/mm for  $25\lambda_{\text{SAW}}$ , 8.15 dB/mm for  $50\lambda_{\text{SAW}}$ , and 7.28 dB/mm for  $75\lambda_{\text{SAW}}$ . These propagation losses are higher than the previously reported loss of 5.9 dB/mm for  $\text{Al}_{0.58}\text{Sc}_{0.42}\text{N}/4\text{H-SiC}$ , which may be a result of surface roughening in our devices [29]. Based on these results, a device aperture of  $75\lambda_{\text{SAW}}$  was selected for our acoustic-driven magnetic resonance experiments. Using a representative SAW device, we calculated the electromechanical coupling coefficient,  $k^2$ , as 4.47% and 1.79% for the Sezawa and Rayleigh modes, respectively,

which effectively agrees with the 4.38% and 1.11% determined from the COMSOL simulations (the corresponding data and analysis can be found in Supplemental Material 4) [50,52].

#### IV. ADMR DEVICE FABRICATION AND PERFORMANCE

Following the characterization and optimization of the SAW delay line devices based on the Rayleigh and Sezawa modes cosupported in the AlScN/SiC piezoelectric platform, we deposited magnetic strips of the FeGaB/SiO<sub>2</sub>/FeGaB heterostructure with an *in-situ* magnetic bias field at 45° relative to the SAW device propagation axis (fabrication details can be found in Supplemental Material 5) [50]. A representative ADMR device is shown in Fig. 5. Following a scanning electron microscopy inspection, the fabricated devices were found to be close to the desired periodicity with a wavelength of  $2.210 \mu\text{m}$ .

The SAWs are generated through an applied microwave signal via rf probes in a ground-signal-ground configuration to the interdigital transducers. As the SAWs propagate through the magnetic heterostructure, the lattice oscillations and strain induce an effective rf magnetic field. Under a static in-plane magnetic field ( $H_x$ ,  $H_y$ ), spin waves are excited, resulting in magnetoacoustic transduction that produces both SAW attenuation and delay. We applied the static magnetic field via nested Helmholtz coils with bipolar power supplies to produce an in-plane vector magnetic field. Following a short, open load, through two-port calibration, we used a vector network analyzer to measure attenuation through scattering parameters  $S_{21}$  and  $S_{12}$ , characterizing the transmission of SAWs traveling in the  $+k$  and  $-k$  directions. The difference between the magnitude of the  $S_{21}$  and  $S_{12}$  (dB) defines the transmission nonreciprocity present. The difference between the  $S_{21}$  phase and the  $S_{12}$  phase defines the phase accumulation. Here, we characterized ADMR devices based on FeGaB/SiO<sub>2</sub>/FeGaB grown on an AlScN/SiC platform, specifically with an aperture of  $75\lambda_{\text{SAW}}$  and delay lengths of 50, 250, 500, and  $750 \mu\text{m}$ . The magnetic absorption plots calculated from  $S_{21}$  and  $S_{12}$ , which represent the SAW-induced magnetic resonance as a function of the magnetic bias field (see Fig. 6 for the results for the 500- $\mu\text{m}$  device, where all the plots are provided in Supplemental Materials 6 and 7) [50]. The magnetic absorption plots for the characterized devices had asymmetry because of the uniaxial anisotropy induced during the deposition under the applied magnetic field, which is consistent with previous findings of FeCoSiB with uniaxial anisotropy on Y-cut LiNbO<sub>3</sub> [53]. The magnetic absorption symmetries were four-lobed with narrow resonance linewidths similar to FeGaB on Y-cut LiNbO<sub>3</sub> [53]. The four-lobed absorption symmetry is to be expected for a Rayleigh-like mode due to the in-plane effective ac magnetic field dependence

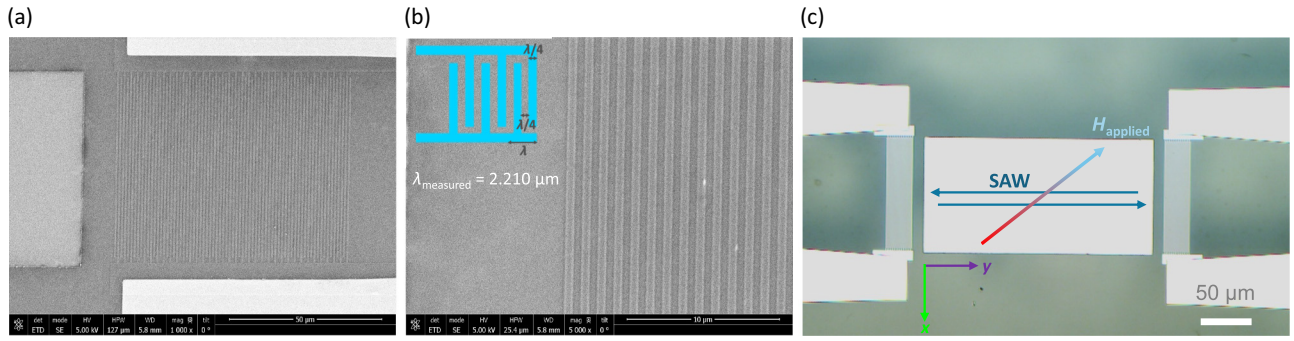


FIG. 5. (a) Representative scanning electron microscopy image of the ADMR device. (b) Representative scanning electron microscopy image of the SAW bidirectional interdigital transducers. (c) Representative optical microscopy image of an ADMR device on AlScN/SiC with the geometry of the ADMR experiments overlaid on the image.

on  $\sin \phi_0 \cos \phi_0$ , as shown by the following expression [11]:

$$\begin{aligned} \mathbf{h}_{\text{eff}}(x, t) &= \begin{pmatrix} h_{\text{out-of-plane}} \\ h_{\text{in-plane}} \end{pmatrix} \\ &= \frac{2}{\mu_0} \begin{pmatrix} (b_2 \varepsilon_{xz} + \frac{\mu_0}{2} M_{\text{eff}} \omega_{xz}) \cos \phi_0 \\ b_1 \varepsilon_{xx} \sin \phi_0 \cos \phi_0 \end{pmatrix} e^{-i(kx - \omega t)}. \end{aligned} \quad (3)$$

In Eq. (3),  $\mu_0$  is the permeability of free space,  $b_1$  and  $b_2$  are the magnetoelastic constants for cubic crystal,  $M_{\text{eff}}$  is the effective magnetization,  $\varepsilon$  is strain, and  $\phi_0$  is the angle between the propagation direction,  $k$ , along the  $x$ -axis, and the equilibrium magnetization direction. Note, for a Rayleigh-like mode, the elliptical lattice motion leads to nonzero strain  $\varepsilon_{xz} \neq 0$  and  $\varepsilon_{xx} \neq 0$ , and  $\omega_{xz} \neq 0$ . The maximum magnetic absorption experimentally determined from  $S_{21}$  for the Rayleigh mode was  $26.4 \pm 2.5$  dB/mm and  $9.5 \pm 1.7$  dB/mm for the Sezawa mode, which is shown in Fig. 7(a). The ADMR delay lines demonstrated significant transmission nonreciprocity, approximately  $7.3 \pm 0.8$  dB/mm for the Rayleigh mode and  $3.3 \pm 0.6$  dB/mm for the Sezawa mode, as shown in

Fig. 6 (just the 500- $\mu\text{m}$  device is shown), Fig. 7 (plotted with maximum nonreciprocity as a function of delay length and the corresponding fit), and Fig. 8 (all nonreciprocity data). This nonreciprocity seems to arise from the helicity mismatch effect, as evidenced by the fact that the absorption symmetry pattern in terms of the magnetic field resonance fields was consistent for  $S_{21}$  and  $S_{12}$ , whereas if our nonreciprocity were a result of an asymmetric spin wave dispersion, then one propagation direction would have a lower resonance field than the opposite propagation direction—an example of the different origins of ADMR nonreciprocity is shown in Fig. 1. The nonreciprocity observed here is also chiral based on the acoustic mode polarization. For an object to be chiral, the object cannot be superimposed onto its mirror image through rotation and translation alone. Here, while the uniaxial anisotropy can be compensated through translation, if you rotate the absorption patterns in Figs. 6(a) and 6(b), then the lobes labeled 1 and 2 cannot be superimposed onto the lobes labeled 3 and 4. Therefore, they do not have  $180^\circ$  rotational symmetry and the effect is chiral. In further support of the observed chiral nonreciprocity being driven by the helicity mismatch effect is the fact that the handedness of the observed nonreciprocity

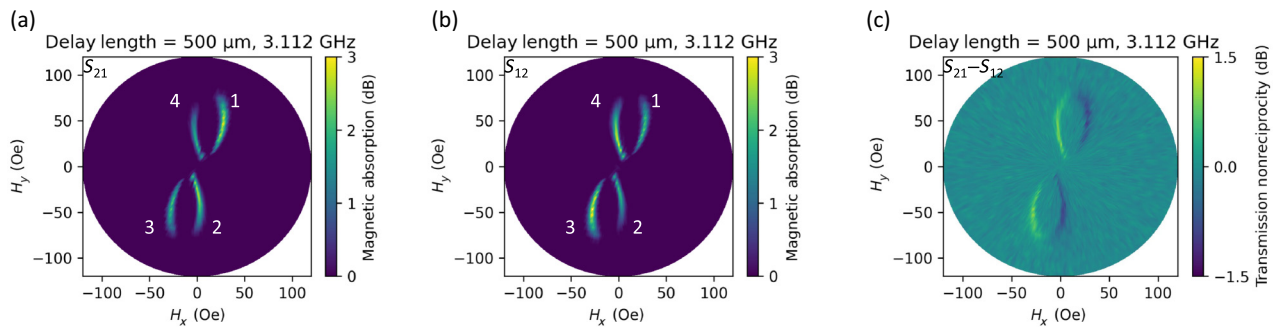


FIG. 6. Magnetic absorption pattern with numbered lobes for the 500- $\mu\text{m}$  delay length device calculated from (a)  $S_{21}$  and (b)  $S_{12}$ . (c) Transmission nonreciprocity,  $S_{21}-S_{12}$  (dB), as a function of the in-plane applied dc magnetic field for the 500- $\mu\text{m}$  delay length device.

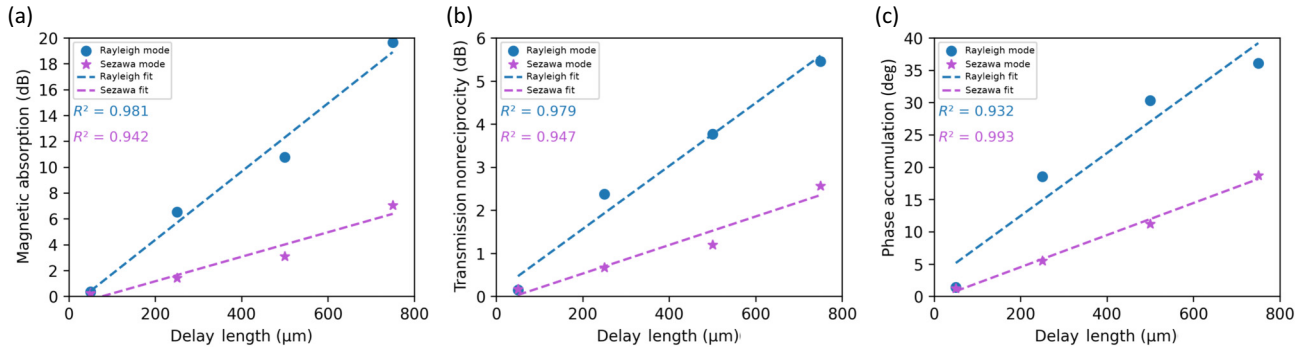


FIG. 7. Experimentally determined (a) maximum magnetic absorption,  $S_{21}(H_x, H_y) - S_{21}(0, 0)$ , for the ADMR delays of varying length, (b) maximum transmission nonreciprocity,  $|S_{21} - S_{12}|_{\text{maximum}}$ , for the ADMR delays of varying length, and (c) maximum phase accumulation,  $|\varphi_{S_{21}} - \varphi_{S_{12}}|_{\text{maximum}}$ , for ADMR delays of varying length.

is switched based on the retrograde versus prograde elliptical particle displacement, which is shown in Fig. 8. In this context, chirality refers to the intrinsic elliptical polarization (particle displacement and velocity spatial pattern) of the acoustic waves, where the propagation direction determines the handedness of the coupled SAW-spin wave interaction. The Rayleigh mode exhibits a retrograde elliptical particle displacement, while the Sezawa mode has a prograde elliptical displacement. This acoustic wave polarization is central to the helicity mismatch effect that depends on the relative orientation of the wavevector and the external magnetic field. In addition to the observed chiral and nonreciprocal transmission of acoustic power, there was a notable phase accumulation (maximum phase accumulation defined as  $|\varphi_{S_{21}} - \varphi_{S_{12}}|_{\text{maximum}}$ ) for these two acoustic modes:  $48.6 \pm 9.3^\circ/\text{mm}$  for the Rayleigh mode and  $24.8 \pm 1.5^\circ/\text{mm}$  for the Sezawa mode (see Fig. 7 and Supplemental Material 8) [50]. A three-element phase

interference-based circulator relies on achieving a  $180^\circ$  round-trip phase difference, which ensures that signals constructively interfere in the forward direction while canceling out in the reverse direction, thereby enabling nonreciprocal circulation of the acoustic wave between the ports. For implementing a three-element phase-interference-based circulator, a phase accumulation of  $60^\circ$  per element is necessary, which corresponds to a length of 1.233 mm per nonreciprocal element for the Rayleigh mode. Given this required interaction length, an interaction-related loss of 33 dB per element would be expected; however, this loss could potentially be offset using an integrated acoustoelectric amplifier [34,54]. Increased phase accumulation per interaction length, which would reduce the size and loss of a proposed interference-based circulator, could be achieved through optimized synthetic antiferromagnetic heterostructures with tuned interlayer dipolar coupling strength [24].

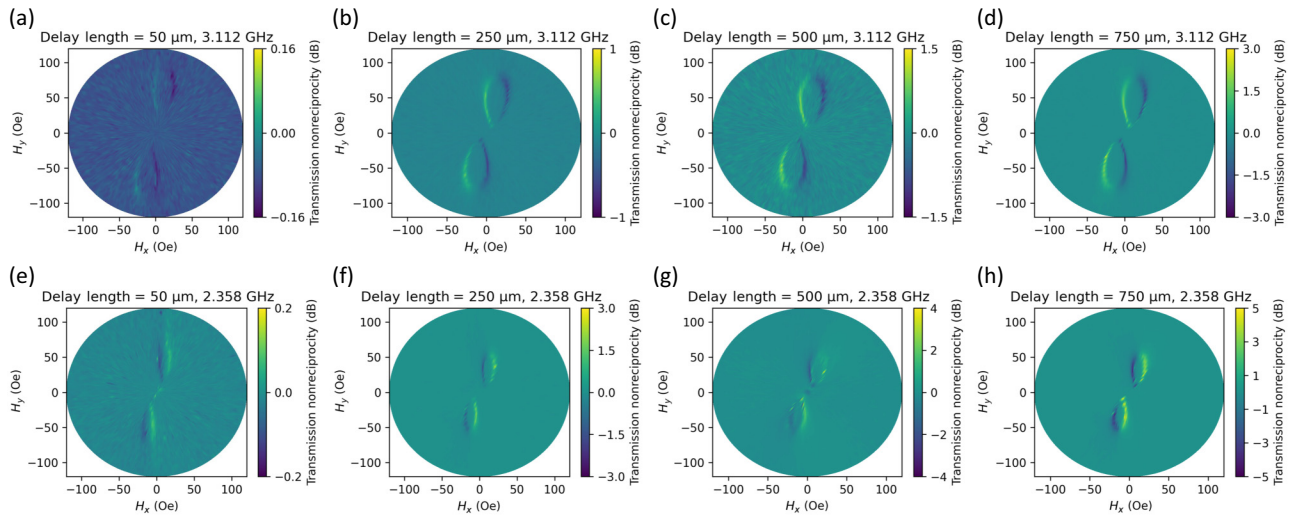


FIG. 8. Transmission nonreciprocity,  $S_{21} - S_{12}$  (dB), as a function of the in-plane applied dc magnetic field (Oe) for the Sezawa mode with a delay length of (a) 50  $\mu\text{m}$ , (b) 250  $\mu\text{m}$ , (c) 500  $\mu\text{m}$ , and (d) 750  $\mu\text{m}$ , and for the Rayleigh mode with a delay length of (e) 50  $\mu\text{m}$ , (f) 250  $\mu\text{m}$ , (g) 500  $\mu\text{m}$ , and (h) 750  $\mu\text{m}$ .

## V. SUMMARY AND CONCLUSIONS

In this study, we engineered a piezoelectric AlScN/SiC platform to support two helicities of acoustic polarizations, i.e., Rayleigh and Sezawa SAWs, and demonstrated chiral nonreciprocal coupling between these SAWs and spin waves in a FeGaB/SiO<sub>2</sub>/FeGaB heterostructure driven by the helicity mismatch effect. The FeGaB/SiO<sub>2</sub>/FeGaB heterostructure was thoroughly characterized using polarized neutron reflectometry and broadband ferromagnetic resonance measurements. These confirmed high-quality FeGaB deposition with a high effective magnetization, negligible inhomogeneous broadening, and low magnetic damping. The SAW devices fabricated on the AlScN/SiC platform supported both the Rayleigh and Sezawa modes and the transducer was optimized such that the bidirectional IDTs achieved a Sezawa mode insertion loss close to the intrinsic limit of 6 dB. Scattering parameters were characterized under varying in-plane magnetic fields ( $H_x$ ,  $H_y$ ) using rf probes in a ground-signal-ground configuration, eliminating the need for wire bonding. The magnetic absorption spectra revealed four-lobe resonances with slight asymmetry due to uniaxial anisotropy, consistent with prior studies. Strong chiral nonreciprocity in magnetoacoustic wave transmission was observed, marked by a broken rotational symmetry. This arises from the helicity mismatch between the spin wave and either the retrograde elliptical Rayleigh mode or the prograde elliptical Sezawa mode. The Rayleigh mode at 2.358 GHz showed stronger magnetic absorption, greater nonreciprocal transmission, and more significant phase accumulation compared with the Sezawa mode at 3.112 GHz, potentially due to the frequency-dependent behavior of the SAW-spin-wave interaction. Further frequency-dependent studies of the Rayleigh and Sezawa modes are required to elucidate this fact. To further advance this research, it is essential to develop a comprehensive model that accurately captures the various contributions to a SAW-spin-wave coupling. This model should include contributions such as the helicity mismatch effect, spin wave dispersion engineering, and the influence of different acoustic mode polarizations. Such an approach could enable the ability to predict maximal nonreciprocity in these systems. Notably, there has been progress in creating a COMSOL-based micromagnetic simulation module that solves the Landau-Lifshitz-Gilbert equation in the frequency domain, allowing for the determination of spin wave eigenmodes and their corresponding dispersions [55,56]. By integrating this simulation with the ACOUSTICS module, it would be possible to predict the coupled SAW-spin-wave eigenmodes and their dispersion characteristics, providing a powerful tool for harnessing these interactions in next-generation radiofrequency and microwave devices. In conclusion, this platform, with its high electromechanical coupling efficiency, isotropic in-plane acoustic behavior, and excellent thermal

conductivity, is ideal for compact, frequency-selective, nonreciprocal radiofrequency and microwave components, such as isolators and circulators.

## ACKNOWLEDGMENTS

This project was funded in part by the DARPA Young Faculty Award program. A portion of this research used resources at Sandia National Laboratories. Sandia National Laboratories is a multimission laboratory managed and operated by National Technology & Engineering Solutions of Sandia, LLC, a wholly owned subsidiary of Honeywell International Inc., for the U.S. Department of Energy's National Nuclear Security Administration under contract DE-NA0003525. This work was performed, in part, at the Center for Integrated Nanotechnologies, an Office of Science User Facility operated for the U.S. Department of Energy (DOE) Office of Science.

Any subjective views or opinions that might be expressed in the paper do not necessarily represent the views of the U.S. Department of Energy or the United States Government. A portion of this research used resources at the Spallation Neutron Source, a DOE Office of Science User Facility operated by the Oak Ridge National Laboratory. Certain commercial equipment, instruments, software, or materials are identified in this paper in order to specify the experimental procedure adequately. Such identifications are not intended to imply recommendation or endorsement by NIST, nor are they intended to imply that the materials or equipment identified are necessarily the best available for the purpose. Additionally, any subjective views or opinions that might be expressed in the paper do not necessarily represent the views of NIST.

- 
- [1] G. A. Petsko, On the other hand, *Science* **256**, 1403 (1992).
  - [2] R. E. Franklin and R. G. Gosling, Molecular configuration in sodium thymonucleate, *Nature* **171** (4356), 740 (1953).
  - [3] J. D. Watson and F. H. C. Crick, A structure of deoxyribose nucleic acid, *Nature* **171** (4356), 737 (1953).
  - [4] L. Pauling, R. B. Corey, and H. R. Branson, The structure of proteins: two hydrogen-bonded helical configurations of the polypeptide chain, *Proc. Natl. Acad. Sci. U. S. A.* **37** (4), 205 (1951).
  - [5] G. N. Ramachandran, C. Ramakrishnan, and V. Sasisekharan, Stereochemistry of polypeptide chain configurations, *J. Mol. Biol.* **7** (1), 95 (1963).
  - [6] A. Fresnel, Memoir on the law of the modifications that reflection impresses on polarized light, *Mem. Submitted Fr. Acad. Sci.* **7**, 549 (1822).
  - [7] J. D. Jackson, *Classical Electrodynamics*, 3rd ed. (Wiley, New York, USA, 1998).
  - [8] B. A. Auld, *Acoustic Fields and Waves in Solids* (John Wiley & Sons, New York, USA, 1973), Vol. 1.

- [9] B. A. Auld, *Acoustic Fields and Waves in Solids* (John Wiley & Sons, New York, USA, 1973), Vol. 2.
- [10] V. V. Kruglyak, S. O. Demokritov, and D. Grundler, Magnonics, *J. Phys. D: Appl. Phys.* **43** (26), 264001 (2010).
- [11] M. Küß, M. Albrecht, and M. Weiler, Chiral magnetoacoustics, *Front. Phys.* **10**, 1 (2022).
- [12] M. F. Lewis and E. Patterson, Acoustic-surface-wave isolator, *Appl. Phys. Lett.* **20**, 276 (1972).
- [13] R. Sasaki, Y. Nii, Y. Iguchi, and Y. Onose, Nonreciprocal propagation of surface acoustic wave in Ni/LiNbO<sub>3</sub>, *Phys. Rev. B* **95**, 020407(R) (2017).
- [14] M. Xu, K. Yamamoto, J. Puebla, K. Baumgaertl, B. Rana, K. Miura, H. Takahashi, D. Grundler, S. Maekawa, and Y. Otani, Nonreciprocal surface acoustic wave propagation via magneto-rotational coupling, *Sci. Adv.* **6**, eabb1724 (2020).
- [15] J. Puebla, Y. Hwang, S. Maekawa, and Y. Otani, Perspectives on spintronics with surface acoustic waves, *Appl. Phys. Lett.* **120**, 220502 (2022).
- [16] S. Maekawa and M. Tachiki, *AIP Conf. Proc.* **29**, 542 (2008).
- [17] M. Matsuo, J. Ieda, K. Harii, E. Saitoh, and S. Maekawa, Mechanical generation of spin current by spin-rotation coupling, *Phys. Rev. B* **87**, 180402, (2013).
- [18] D. Kobayashi, T. Yoshikawa, M. Matsuo, R. Iguchi, S. Maekawa, E. Saitoh, and Y. Nozaki, Spin current generation using a surface acoustic wave generated via spin-rotation coupling, *Phys. Rev. Lett.* **119**, 077202 (2017).
- [19] Y. Kurimune, M. Matsuo, and Y. Nozaki, Observation of gyromagnetic spin wave resonance in NiFe films, *Phys. Rev. Lett.* **124**, 217205 (2020).
- [20] A. R. Will-Cole, A. E. Hassanien, S. Deniz Caliskan, M.-G. Jeong, X. Liang, S. Kang, V. Rajaram, I. Martos-Repeth, H. Chen, A. Risso, *et al.* Tutorial: Piezoelectric and magneto-electric N/MEMS – Materials, devices, and applications, *J. Appl. Phys.* **131**, 241101 (2022).
- [21] B. Luo, A. R. Will-Cole, C. Dong, Y. He, X. Liu, H. Lin, R. Huang, X. Shi, M. McConney, M. Page, *et al.*, Magneto-electric microelectromechanical and nanoelectromechanical systems for the IoT, *Nat. Rev. Electr. Eng.* **1**, 317 (2024).
- [22] P. Shah, D. A. Bas, I. Lisenkov, A. Matyushov, N. X. Sun, and M. R. Page, Giant nonreciprocity of surface acoustic waves enabled by the magnetoelastic interaction, *Sci. Adv.* **6**, eabc5648 (2020).
- [23] M. Küß, M. Heigl, L. Flacke, A. Hörner, M. Weiler, M. Albrecht, and A. Wixforth, Nonreciprocal Dzyaloshinskii-Moriya magnetoacoustic waves, *Phys. Rev. Lett.* **125**, 21720 (2020).
- [24] D. A. Bas, R. Verba, P. J. Shah, S. Leontsev, A. Matyushov, M. J. Newburger, N. X. Sun, V. Tyberkevich, A. Slavin, and M. R. Page, Nonreciprocity of phase accumulation and propagation losses of surface acoustic waves in hybrid magnetoelastic heterostructures, *Phys. Rev. Appl.* **18**, 044003 (2022).
- [25] M. Küß, M. Hassan, Y. Kunz, A. Hörner, M. Weiler, and M. Albrecht, Nonreciprocal magnetoacoustic waves in synthetic antiferromagnets with Dzyaloshinskii-Moriya interaction, *Phys. Rev. B* **107**, 0244 (2023).
- [26] M. Küß, S. Glamsch, Y. Kunz, A. Hörner, M. Weiler, and M. Albrecht, Giant surface acoustic wave nonreciprocity with low magnetoacoustic insertion loss in CoFeB/Ru/CoFeB synthetic antiferromagnets, *ACS Appl. Electron. Mater.* **5** (9), 5103 (2023).
- [27] M. Küß, S. Glamsch, A. Hörner, and M. Albrecht, Wideband, nonreciprocal transmission of surface acoustic waves in synthetic antiferromagnets, *ACS Appl. Electron. Mater.* **6** (3), 1790 (2024).
- [28] R. Verba, E. N. Bankowski, T. J. Meitzler, V. Tiberkevich, and A. Slavin, Phase non-reciprocity of microwave-frequency surface acoustic waves in hybrid heterostructures with magnetoelastic coupling, *Adv. Electron. Mater.* **7**, 2100263 (2021).
- [29] X. Du, Z. Tang, C. Leblanc, D. Jariwala, and R. H. Olsson, in *2022 Joint Conference of the European Frequency and Time Forum and IEEE International Frequency Control Symposium (EFTF/IFCS), Paris, France* (2022), pp. 1–2.
- [30] X. Du, N. Sharma, Z. Tang, C. Leblanc, D. Jariwala, and R. H. Olsson, A 6-GHz Sezawa mode surface acoustic wave resonators using AlScN on SiC, *J. Microelectromech. Syst.* **33** (5), 577 (2024).
- [31] S. Lotfi, L.-G. Li, Ö Vallin, L. Vestling, H. Norström, and J. Olsson, LDMOS-transistors on semi-insulating silicon-on-polycrystalline-silicon carbide substrates for improved RF and thermal properties, *Solid-State Electron.* **70**, 14 (2012).
- [32] Z. Yang, F. Wang, W. Nie, X. Han, X. Guo, X. Shan, X. Lin, H. Dun, Z. Sun, Y. Xie, and K. Zhang, Surface acoustic wave temperature sensor based on Pt/AlN/4H-SiC structure for high temperature environments, *Sens. Actuators, A* **357**, 114379 (2023).
- [33] M. Liffredo, S. Stettler, F. Peretti, and L. Guillermo Villanueva, Rayleigh wave suppression in Al<sub>0.6</sub>Sc<sub>0.4</sub>N-on-SiC resonators, arXiv:2407.20286 [cond-mat.mtrl-sci], (2024).
- [34] L. Hackett, X. Du, M. Miller, B. Smith, S. Santillan, J. Montoya, R. Reyna, S. Arterburn, S. Weatherred, T. A. Freidmann, R. H. Olsson, and M. Eichenfield, S-band acoustoelectric amplifier in an InGaAs-AlScN-SiC architecture, *Appl. Phys. Lett.* **124**, 113503 (2024).
- [35] J. Lou, R. E. Insignares, Z. Cai, K. S. Ziemer, M. Liu, and N. X. Sun, Soft magnetism, magnetostriction, and microwave properties of FeGaB thin films, *Appl. Phys. Lett.* **91**, 182504 (2007).
- [36] A. R. Will-Cole, A. Gilad Kusne, P. Tonner, C. Dong, X. Liang, H. Chen, and N. X. Sun, Application of Bayesian optimization and regression analysis to ferromagnetic materials development, *IEEE Trans. Magn.* **58** (1), 1 (2022).
- [37] C. Dong, M. Li, X. Liang, H. Chen, H. Zhou, X. Wang, Y. Gao, M. E. McConney, J. G. Jones, G. J. Brown, B. M. Howe, and N. X. Sun, Characterization of magnetomechanical properties in FeGaB thin films, *Appl. Phys. Lett.* **113**, 262401 (2018).
- [38] V. Lauter, H. Ambaye, R. Goyette, W-T. Hal Lee, and A. Parizzi, Highlights from the magnetism reflectometer at the SNS, *Phys. B: Condens. Matter* **404** (17), 2543 (2009).
- [39] J. F. Ankner and G. P. Felcher, Polarized-neutron reflectometry, *J. Magn. Magn. Mater.* **200** (1–3), 741 (1999).
- [40] V. Lauter-Pasyuk, Neutron grazing incidence techniques for nano-science, *SFN* **7**, s221 (2007).

- [41] H. J. C. Lauter and B. P. Toperverg, in *Polymer Science: A Comprehensive Reference*, edited by K. Matyjaszewski, and M. Möller (Elsevier, Oxford, UK, 2012), pp. 411–432. ISBN 9780080878621
- [42] P.A. Kienzle, B.B. Maranville, K.V. O'Donovan, J.F. Ankner, N.F. Berk, and C.F. Majkrzak, <https://www.nist.gov/ncnr/reflectometry-software>, (2017).
- [43] P. Ntetsika, G. Mitrikas, G. Litsardakis, and I. Panagiotopoulos, Mixing of acoustic and optical excitations in Ru/Co based multilayers, *Mater. Adv.* **3**, 5451 (2022).
- [44] G. W. Farnell and E. L. Adler, in *Physical Acoustics*, edited by W. P. Mason, and R. N. Thurston (Academic Press, New York, USA, 1972), Vol. 9, pp. 35–127.
- [45] J. W. Grate, S. J. Martin, and R. M. White, Acoustic wave microsensors. Part II, *Anal. Chem.* **65**, 987A (1993).
- [46] F. Hadj-Larbi and R. Serhane, Sezawa SAW devices: Review of numerical-experimental studies and recent applications, *Sens. Actuators, A* **292**, 169 (2019).
- [47] A. T. Tarekegne, B. Zhou, K. Kaltenecker, K. Iwaszczuk, S. Clark, and P. U. Jepsen, Terahertz time-domain spectroscopy of zone-folded acoustic phonons in 4H and 6H silicon carbide, *Opt. Express* **27** (3), 3618, (2019).
- [48] I. Zdru, C. Nastase, L. N. Hess, F. Ciubotaru, A. Nicoloiu, D. Vasilache, M. Dekkers, M. Geilen, C. Ciornei, A. Dinescu, C. Adelman, M. Weiler, P. Pirro, and A. Müller, A GHz operating CMOS compatible ScAlN based SAW resonator used for Surface Acoustic Waves/Spin Waves Coupling, *IEEE Electron Device Lett.* **43** (9), 1551 (2022).
- [49] A. Nicoloiu, C. Nastase, I. Zdru, D. Vasilache, G. Boldeiu, M. C. Ciornei, A. Dinescu, and A. Müller, in *2021 International Semiconductor Conference (CAS), Romania* (2021), pp. 67–70.
- [50] See Supplemental Material at <http://link.aps.org/supplemental/10.1103/PhysRevApplied.23.034058> for x-ray characterization of the aluminum scandium nitride film, analytical magnetic spin wave dispersions, interdigital transducer surface acoustic wave device optimization, electromechanical coupling analysis, device fabrication flow, and acoustic-driven magnetic resonance characterization for delay lines of length 50, 250, 500, and 750  $\mu\text{m}$ .
- [51] M. G. Cottam, *Linear and Nonlinear Spin Waves in Magnetic Films and Superlattices* (World Scientific, London, UK, 1994).
- [52] L. Hackett, M. Miller, C. M. Nordquist, J. C. Taylor, S. Santillan, R. H. Olsson, and M. Eichenfield, Aluminum scandium nitride films for piezoelectric transduction into silicon at gigahertz frequencies, *Appl. Phys. Lett.* **123** (7), 1 (2023).
- [53] D. A. Bas, P. J. Shah, A. Matyushov, M. Popov, V. Schell, R. C. Budhani, G. Srinivasan, E. Quandt, N. Sun, and M. R. Page, Acoustically driven ferromagnetic resonance in diverse ferromagnetic thin films, *IEEE Trans. Magn.* **57** (2), 4300605 (2021).
- [54] L. Hackett, M. Miller, S. Weatherred, S. Arterburn, M. J. Storey, G. Peke, D. Dominguez, P. S. Finnegan, T. A. Friedmann, and M. Eichenfield, Non-reciprocal acoustoelectric microwave amplifiers with net gain and low noise in continuous operation, *Nat. Electron.* **6**, 76 (2023).
- [55] V. G. Bar'yakhtar and B. A. Ivanov, The Landau-Lifshitz equation: 80 years of history, advances, and prospects, *Low Temp. Phys.* **41**, 663 (2015).
- [56] J. Zhang, W. Yu, X. Chen, and J. Xiao, A frequency-domain micromagnetic simulation module based on COMSOL Multiphysics, *AIP Adv.* **13**, 055108 (2023).